Journal of Analytical and Applied Pyrolysis 132 (2018) 19–32

Contents lists available at ScienceDirect

Journal of Analytical and Applied Pyrolysis

journal homepage: www.elsevier.com/locate/jaap

A novel solar powered biomass pyrolysis reactor for producing fuels and chemicals

Asif H. Rony[a], Daniel Mosiman[b], Zhao Sun[a], Dengfeng Qin[c], Yuan Zheng[b], John H. Boman IV[d], Maohong Fan[a,c,e,*]

[a] Department of Chemical Engineering, University of Wyoming, Laramie, WY 82071, USA
[b] Department of Mechanical Engineering, University of Wyoming, Laramie, WY 82071, USA
[c] Department of Petroleum Engineering, University of Wyoming, Laramie, WY 82071, USA
[d] Department of Sociology, Bowling Green State University, Bowling Green, OH 43403, USA
[e] School of Energy Resources, University of Wyoming, Laramie, WY 82071, USA

ARTICLE INFO

Keywords:
Concentrated solar simulator
Solar flux map
Solar biomass pyrolysis
Bio-oil

ABSTRACT

In this work, a novel pyrolysis reaction system based on a concentrated solar simulator was designed by using a modified 5 kW cinema projector along with supporting components, modeled, and tested for generating bio-based materials including fuels and chemicals in a quartz glass reactor. A corresponding system for measuring the radiation profile produced by the solar simulator was developed. Furthermore, a series of flux maps was modeled with soltrace® to compare the experimental data with the theoretically derived counterparts. The solar simulator produced a peak solar intensity of over 700 suns in a 10 mm diameter area. The temporal variance for flux is within ± 5%. A condensing system which can separate the liquid products at four different temperatures was also designed and constructed. The optimum temperature for maximum bio-oil production was 750 °C measured at the front of the reactor under direct irradiation of solar light. The produced bio-oil, bio-char and gases were analyzed with different instruments such as Fourier-transform infrared spectroscopy (FTIR), gas chromatography (micro-GC), and mass spectroscopy (GC–MS). The effects of solar light intensities on bio-oil composition were studied. Also, solar based pyrolysis was compared with conventional thermal based biomass pyrolysis. The scheme developed in this research opens a new pathway for renewable energy production with solar energy.

1. Introduction

The demand for renewable energy has been increasing [1] despite of the majority of the world energy market is still being dominated by fossil fuel [2,3]. Among the sustainable sources of energy, solar energy – the primary source of energy on earth – is recently gaining considerable attention for low environmental impact [4,5], ease in access [6], social benefits [6,7], longevity [8]. The most inherent issue regarding solar energy production is its unavailability during the night and interrupted supply during a cloudy day are needed to be addressed. A lot of solar researchers have used solar simulators since the 1960s to eliminate the variability [9–11]. Among many alternatives for solar simulators, several key features such as time stability, optical resembles, and spatial distribution of solar flux, are considered to be important while selecting a specific model.

In general, solar simulators can be classified into three categories (A, B, C) [12]. The rating of a solar simulator depends on the light source and type of concentrator. Among the light sources, Xenon arc lamps are widely used for their capability to produce light similar to terrestrial sunlight, their stable spectral characteristics independent of power variation, and their ability to produce a brighter point source than other alternatives [13]. There are several types of concentrators used in research including but not limited to ellipsoidal concentrators, parabolic dish concentrators, Compound parabolic concentrators (CPC), Hyperboloid concentrators, and Fresnel lenses. For concentrated solar power (CSP) applications, parabolic dish concentrators are popular for their ability to focus parallel light on a certain point [14]. Parabolic dish concentrators are emerging as popular in research involving moderate to high temperature [15].

On the other hand, utilization of biomass energy as a sustainable alternative to traditional fossil fuel is also gaining momentum [16] for being environmentally friendly [17], abundant, and carrying the ability to replace traditional fuel [10]. Among the two varieties of the bio-fuel technology, thermochemical and biochemical, thermochemical

* Corresponding author at: Department of Chemical Engineering, University of Wyoming, Laramie, WY 82071, USA.
E-mail address: mfan@uwyo.edu (M. Fan).

https://doi.org/10.1016/j.jaap.2018.03.020
Received 11 January 2018; Received in revised form 22 March 2018; Accepted 22 March 2018
Available online 26 March 2018
0165-2370/

Nomenclature

λ	Wavelength (m)	$E_{b\lambda}$	Blackbody irradiance (W/m^2)
α_λ	Spectral absorptance of the coating material	Q_s	Actual power absorption (W)
ρ_λ	Reflectance of mirror	$G_{b\lambda}$	Solar spectral irradiance (W/m^2)
A	Front area of sensor (m^2)	ρ_λ	Spectral reflectance of the mirror
Q_b	Blackbody power absorption (W)	t_{ins}	Temporal radiation instability (%)
		E_{max}	Maximum solar flux (W/m^2)
		E_{min}	Minimum solar flux (W/m^2)

processes have shown higher conversion efficiency [15]. The conversion reaction can be generalized by equation 1 for carbonaceous material [9,18].

$$C_xH_yO_zX_uN_v \xrightarrow{Heat} CO + CO_2 + H_2 + CH_4 + C_nH_m + H_2O + tar + char \quad (1)$$

In the case of biomass pyrolysis, product distribution is affected mostly by heating rate, temperature, and particle size [19,20]. The reviews by Bridgwater [16] and Tao et al. [21] are very useful for conventional pyrolysis process. However, the additional external heating needed to conduct this process generally supplied by non-sustainable sources making the entire process carbon positive. To address this issue, solar pyrolysis of biomass is viewed as a lucrative option. Many researchers reported the advantages of concentrated solar powered technologies for gasification processes. Liejin et al. [22] described a pilot-scale supercritical water gasification using concentrated solar energy. They proposed a thermodynamic cycle with higher efficiency and zero emission. Jingwei et al. [23] described the production of hydrogen using concentrated solar energy and described the benefits of using concentrated solar energy. Solar biomass pyrolysis, like any other typical pyrolysis process, operates under inert conditions for avoiding oxidation; however, it is powered by concentrated solar energy. Generally, the heat can be transferred to the pyrolysis reactor either by direct irradiance or a heat transfer fluid such as molten salt or via the wall. Although, experimental work related to solar powered pyrolysis of biomass is still very limited, researchers are investigating the impact of heat flux, heating rate, and temperature for various biomasses as reviewed by Kuo et al. [4].

The emphasis in this work was to develop a solar simulator from a cinema projector and use it for directly irradiated solar pyrolysis. We have also designed and constructed other related components such as a solar radiation measurement instrument, a double layer quartz glass reactor for both fixed and fluidized bed thermal conversion processes. After calibrating the solar simulator, we have performed solar pyrolysis of pine sawdust, as a representative biomass. In this paper, fixed bed pyrolysis under direct solar irradiation was studied for the simplicity of operation. The pyrolysis products were analyzed for different temperature and solar flux.

2. Materials and methods

2.1. Sample preparation and characterization

Pine sawdust, used as feed, was collected from beetle killed pine trees from a portion of the Rocky Mountains known as the Snowy Range, in Wyoming, USA. The pinewood was chopped, crushed, milled, and sieved. For solar pyrolysis experiments, 0.5 mm particle size was used.

The proximate and ultimate analyses were performed three times and average values are reported in Table 1. Proximate analysis was performed following ASTM D3172–13 using a TGA – SDT Q600 [24]. The ultimate analysis was performed by a 'Vario MACRO Cube CHNOS Elemental Analyzer'. The details regarding methodology are available in sub-section titled as '2.5 Methodology'.

2.2. Solar power pyrolysis apparatus

The major parts of the solar pyrolysis equipment consist of the solar simulator equipped with a xenon bulb, the calibration system, and a quartz glass reactor.

2.2.1. Solar simulator

A cinema projector, remodeled as a solar simulator, was used as a power source for thermochemical conversion instead of the real sun. It contains a 'Strong International Ultra-80 cinema lamp-house', a rectifier, a high-rise soft ride utility cart, and a scissor lift. The lamp-house positions a xenon arc lamp and a deep-dish parabolic concentrator within the housing to create high-intensity solar band radiation and then directs it out through an aperture. The xenon arc lamps demonstrate similarity to real solar radiation incident on the surface of the earth. However, they produce spectral spikes between wavelengths 850 nm and 1050 nm and spectral lowest point at wavelengths below 300 nm. The spikes are blocked using a coating on the parabolic concentrator.

The system utilizes adjustable screw devices to change the position of the focal point as shown in Fig. A1. The regulator is divided into 20 equal portions, as shown in Fig. A2, to fine-tune the focal positioning. The simulator is able to produce solar band radiation with intensities resembling the solar spectral pattern as well as irradiative flux densities ranging between 200 and 700 suns concentration within a small diameter circle. The device is portable, safe to operate, and efficient enough to produce the required radiation profile.

2.2.2. Heat flux calibration system

An in-house radiation flux measurement system, as illustrated in Fig. 1, was built to analyze the spectral intensity between 200 nm and 3000 nm at different vertical and horizontal positions on a plane in front of the solar simulator. The sensor, supported by a backing plate, can be moved along the horizontal and vertical axis to obtain the radiation profile. The backing plate also supports a flow controller which is connected to the cooling water supply of the sensor. In this work, a Gardon-type gauge was used, instead of a calorimeter, due to some inherent advantages, such as short response time, robustness, and ease of calibration. The details of the sensor can be found in Fig. A3. The sensor is a MedTherm 2500 sun capacity radiometer with a 1 cm diameter widow. It was calibrated using the method described by Ballestrín and colleageus [25]. Assuming that the sensor shown in Fig. A3 is a

Table 1
Pinewood characterization.

Proximate analysis	(% by weight)
Fixed carbon	16.61
Volatile	77.64
Moisture	5.49
Ash	0.26
Ultimate analysis	(% by weight)
Carbon	50.33
Hydrogen	6.21
Nitrogen	0.34
Oxygen	43.07
Sulfur	0.05

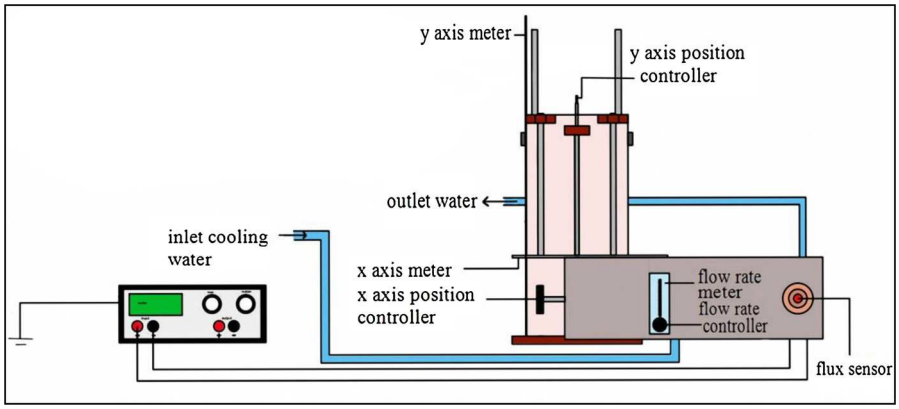

Fig. 1. Heat flux calibration system.

black body, then, the power absorbed by the sensor is

$$Q_b = A \int_{300}^{20000} E_{b\lambda}\alpha_\lambda d\lambda \quad (2)$$

where, A is the area of the sensor, Eβλ is the blackbody irradiance when λ is the wavelength, $\alpha_\lambda$is spectral absorptance of the coating when λ is the wavelength. For a concentrating mirror of reflectance ρ_λ, the actual power absorbed is

$$Q_s = A \int_{300}^{2500} G_{b\lambda}\rho_\lambda\alpha_\lambda d\lambda \quad (3)$$

where, $G_{b\lambda}$is solar spectral irradiance when λ is the wavelength. Q_s is higher than Q_b in practice, so the systematic relative error [26] is defined as $\Delta Q = (Q_s - Q_b)/Q_b$. According to literature, this error is nullified by a 'calibration constant' specific to the coating material. In this study, zynolyte coating was used and the 'calibration constant' for zynolyte is 0.965.

2.2.3. Solar pyrolysis reactor

A cylindrical, two layered, quartz glass reactor with an inner diameter of 29 mm, and an outer diameter of 58 mm was designed. A vacuum was created between the spaces of two layers for better heat retention. A tapering was done in the inner layer to allow placement of fritz, which holds the reactant for thermochemical research. At the focus of the solar simulator, which is inside the reactor and adjacent to the front wall, the temperature was recorded continuously during the operation using a K-type temperature sensor. Another temperature sensor (K-type) was placed at the rear of the reactor, touching the reactor wall to record the rear temperature of the reactor. There were temperature sensors at the inlet and outlet of the reactor as well. This reactor can withstand rapid temperature change up to 1000 °C. It can operate both as fixed and fluidized bed reactor.

2.3. Solar flux model

Soltrace® is widely used for modeling and simulation of solar projects. It utilizes a Monte Carlo ray tracing program [27]. In this method, a large number of solar rays are generated and traveled through the system. The virtual solar system was created using several stages, where each stage was created using elements with specific optical properties [28]. In this work, atmospheric attenuation and tracking errors were not considered. At the end, the flux density distribution is found by counting the number of rays at each grid on the target plane.

2.4. Experimental setup of biomass pyrolysis

The biomass was weighed and placed into the reactor over the fritz. The quartz glass reactor was placed at the focus of the solar simulator and was swept with nitrogen flow controlled by a mass controller as shown in Fig. 2. The sample temperature was measured by a K-type thermocouple measurement. Before the start of the pyrolysis process, safety goggles were worn due to the potential eye damage from intense light. The flux, equivalent to heating rate, was set manually before the test. During the operation, bio-oil is collected at the condenser and stored. After about 30 min, the reaction was practically completed as evidenced from the micro-GC connected at the outlet of the condenser. After the experiment, reactor was cooled down, disassembled, and char was removed. The reactor was rinsed with acetone to collect additional oil and tar deposited on the reactor wall. Each test is run twice and average value is taken when the deviation is within ± 2%.

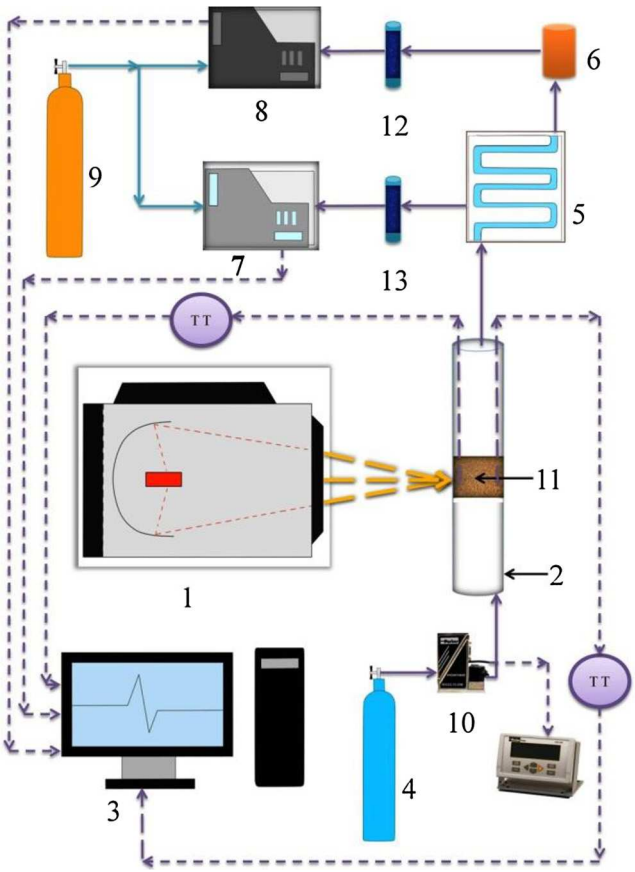

Fig. 2. Solar Pyrolysis Experimental set up. 1-Solar Simulator; 2-Quartz glass reactor; 3-Computer (LabVIEW, GC); 4-Nitrogen Cylinder; 5-Condenser system; 6-Liquid storage; 7-Micro GC; 8-GC-ms; 9-Helium Cylinder; 10-Mass flow controller; 11-Biomass (over fritz); 12 & 13 Moisture trap.

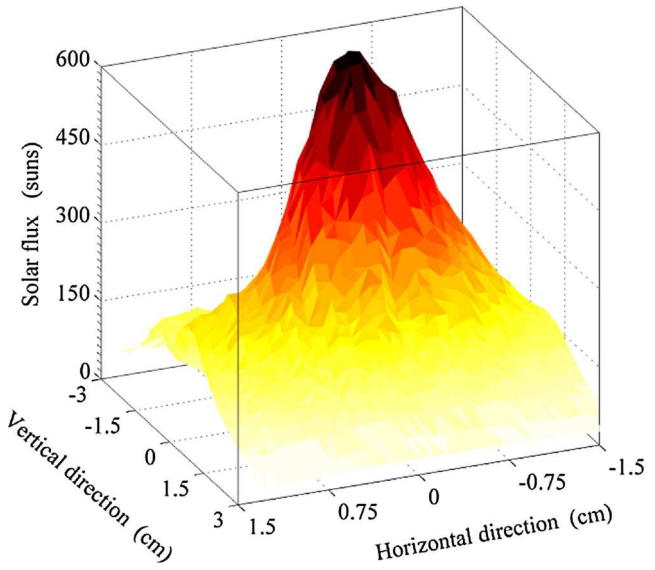

Fig. 3. Solar flux map generated by solar simulator at 170 A. The surface plane was 28.5 cm away from solar simulator.

2.5. Methodology

Several equipments were used to characterize and quantify pyrolysis products including GC-mass spectrometer, micro-GC, FTIR (Fourier Transform Infrared Spectroscopy), TGA (Thermo-gravimetric analysis) and elemental analyzer.

The bio-oil was analyzed by an Agilent 7890B/5977B gas chromatograph/mass spectrometer (GC/MS) with a G4513A ALS auto-injector. An HP-5 MS Ultra Inert capillary column was used for product separation (30 m × 0.25 mm × 0.25 µm). The carrier gas, helium, flow rate was maintained at 1.0 ml/min. During the separation process, the GC column was kept at 40 °C for 3 min before heating up to 40 °C to 300 °C. The heating rate was 3 °C/min and the system kept at 300 °C for 10 min. The number of scans per second for mass spectrometer was 35 amu −550 amu at 70 eV. NIST mass spectral search program for the NIST/EPA/NIH Mass spectral library version 2.2 was used to detect the peaks.

A Varian 490-GC (micro-GC) was used for the analysis of the product gases from pyrolysis. A 10 m Molecular Sieve 5A column for the permanent gas analysis, a 10 m PoraPLOT Q column for the CO_2 analysis were used during the analysis at 70 °C. 'Thermal conductivity detector' (TCD) was used in both of the channels. Helium was used as carrier gas for the GC at 80 psi. The GC pumped in gas samples through a sampling line, heated at 50 °C, connected to the product stream out of the reactor. The runtime was 180s, sampling time was 30 s and stabilization time was 5s. The GC was calibrated for each column using three different gas mixtures with known premixed gas mixtures on the basis of their mole percent.

Fourier-transform infrared spectroscopy (FTIR) analysis was performed using a Nicolet™ iS™ 50 FT-IR Spectrometer. The wave number range of FTIR was 400–4000 cm^{-1}. The resolution was set at 4 cm^{-1} and the number of scans per minute was 32.

Thermogravimetric analysis was performed using TGA-SDT Q600 V20. The heating rate used was 10 K/min from 40 °C to 900 °C under nitrogen environment at atmospheric pressure. At 900 °C sample had been kept for 20 min before air was introduced to the TGA apparatus to burn off the sample. The purge flow rate of nitrogen was 100 ml/min.

A vario® Macro cube CHNOS elemental analyzer performed the elemental composition analysis. The 'coal50' method, available from the manufacturer, was used for analysis. Approximate weights of the samples were 50 mg. All tests were performed at least three times. The sample was burned completely in presence of oxygen and respective oxides of carbon, nitrogen, sulfur, hydrogen were adsorbed in the columns. Ash components were not considered for this analysis. Oxygen was calculated from the balance of other four elements.

3. Results and discussion

3.1. Solar flux map

The solar simulator used in this work can produce stable solar flux at different locations and settings within a short period of time. The solar flux was measured on a different plane in front of the solar simulator. A typical flux contour is shown in Fig. 5. The darker color represents higher solar flux, while lighter color represents lower solar flux. It can be observed that, focusing of solar simulator is crucial for proper pyrolysis experiment. The solar flux map shown in Fig. 3 was measured on a perpendicular plane, 28.5 cm away from the solar simulator. The flux maps for other different power inputs and distances can be found in Figs. A4–A8.

3.2. Effect of time and input power on solar flux

Temporal radiation instability [12] is defined as

$$t_{ins}(\%) = \frac{E_{max} - E_{min}}{E_{max} + E_{min}} * 100\%. \quad (4)$$

Temporal instability is measured at a certain point for a given amount of time. E_{max} defines the maximum solar flux at a certain point for the given amount of time and E_{min} defines the minimum solar flux at a certain point for the given amount of time. In Fig. 4, according to the measured data, after a short period of time (4–5 min), the solar simulator produces very stable solar flux. It can also be stated that the solar flux stabilizes fairly quickly irrespective of location and settings.

The solar flux amount incident on the target plane is dependent on the input power. If the voltage is considered fairly constant, the flux depends on input current (I). The power-flux relationship is a straight-line as seen in Fig. 5. The fluctuations of power are ± 30 W, while the error of solar flux measurements is ± 10 suns. The fluctuations mainly

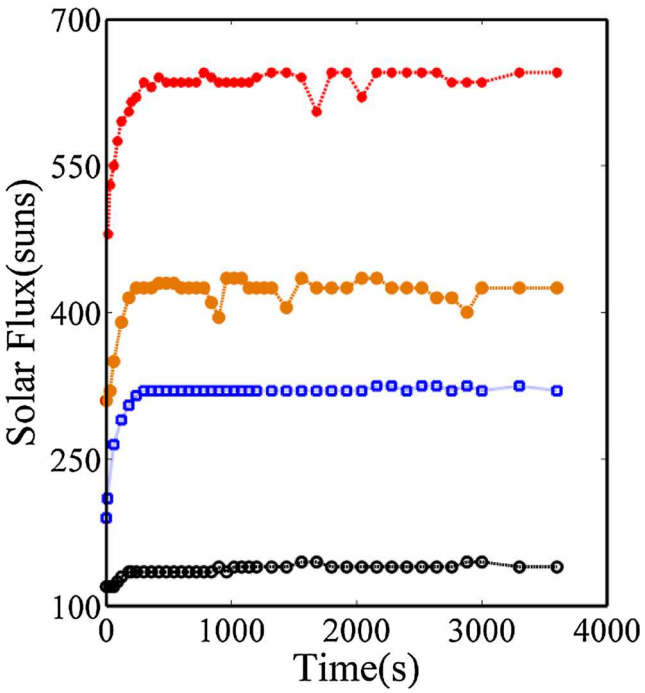

Fig. 4. Simulated Solar Flux Stability over time [a: — 28.5 cm away for 165A; b: — 26.5 cm away for 150A; c: — 30.5 cm away for 130A; d: — 30.5 cm away for 140A]. The voltage can be treated as constant 30 V.

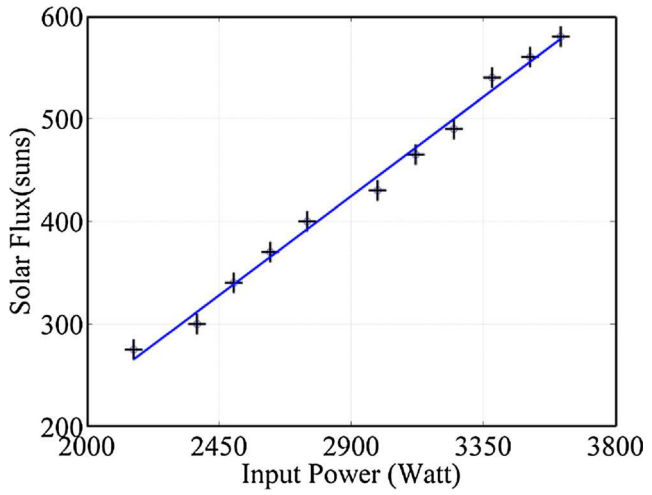

Fig. 5. Solar Flux at Various Input Power of the Solar Simulator. [Y = 0.2149X − 198.72, R^2 = 0.99].

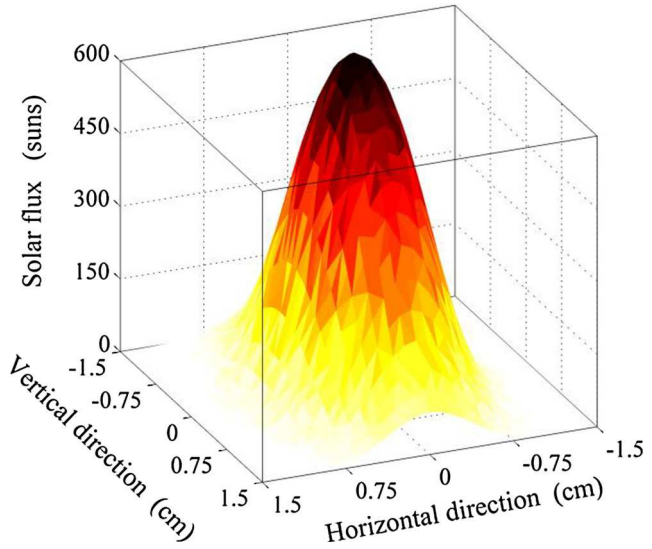

Fig. 6. Solar flux map generated by Soltrace® comparable to Fig. 3. The surface plane was 28.5 cm away from the point source.

originate from the input power supply. The Gardon-gauge used to measure solar flux has a resolution of ± 1A. But, the pattern of the solar flux is similar for different power levels and is virtually independent of the input power.

3.3. Solar flux model

Fig. 6 represents the modeled solar flux map using first principal for the same condition as described for Fig. 3. The model flux map is essentially smooth because practical disturbances were not taken into account. The flux map models for other different power inputs (concentration ratio) and distances can be found in Figs. A9–A13.

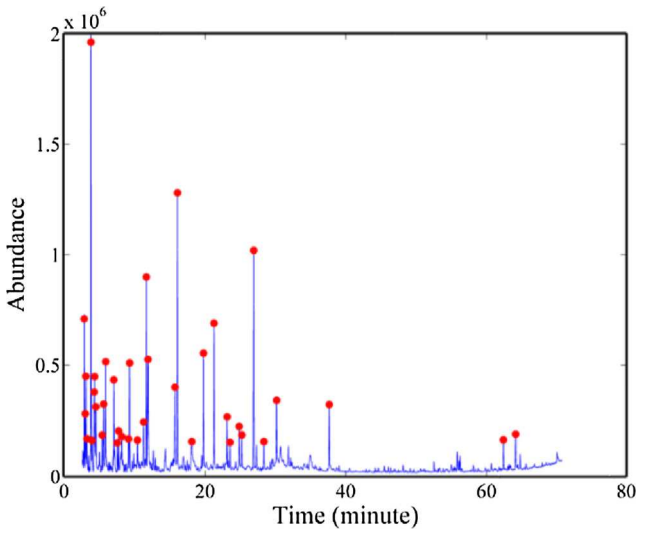

Fig. 8. Mass spectrum of solar pyrolysis bio-oil. The oil was collected for pinewood pyrolysis under 301 suns flux intensity.

3.4. Effect of solar flux on bio-oil production

Fig. 7a shows the effect solar flux on bio-oil production and overall production. In a fixed bed reactor, the conversion can be incomplete. The conversion rate was maximized for bio-oil production at 301 suns, but the overall conversion rate was highest at 355 suns. Fig. 7b, shows the temperature profile over time at different solar flux. The front temperatures, denoted by the solid lines, reached the steady state within 100 s but rear temperatures, denoted by the broken lines, reached the steady state rather slowly. The average temperature and 'heating rate' were always higher when the solar flux was increased. For our system, the 'solar flux' replaces the terms 'heating rate' and 'operating temperature'. The temperatures of the system could reach more than 900 °C with the solar simulator, although they were not utilized for this solar pyrolysis research. The reason for not doing so was to prevent possible damage of quartz glass material and yield more bio-oil at a lower temperature as demonstrated in Fig. 7a and b. Morales et al. described the energy balances for a similar solar powered system [15]. At higher solar flux, tar development on the reactor wall was faster and the reaction slowed down quicker when compared to a lower solar flux.

3.5. Product characterization

The liquid product from the solar pyrolysis is bio-oil, which can be

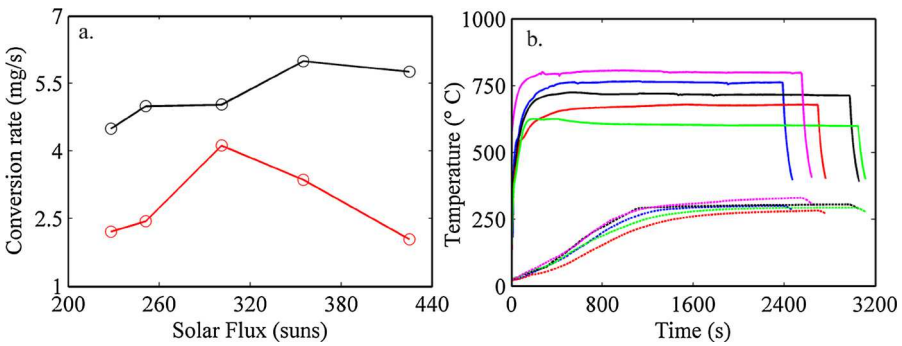

Fig. 7. Solar Thermal conversion of Pine saw dust. a) Conversion rate of biomass at different solar flux intensity [— Overall conversion of pine sawdust; — Conversion to liquid of pine sawdust]; b) Temperature profile at the front (solid lines) and rear (broken line) of the quartz reactor under different flux intensity [— 425 suns; —355 suns; —301 suns; —251 suns; — 228 suns].

Table 2
Bio-oil compound produced from pine sawdust at 301 suns intensity.

	Reten-tion time	Compound	Molecular Formula	Mole-cular Weight	Classification	Functional Group
1	2.87	2-chloropropane	C_3H_7Cl	78.54	Acyclic	halogen
2	3.02	butanedial	$C_4H_6O_2$	86.09	Acyclic	aldehyde
3	3.11	methyl 2-oxopropanoate	$C_4H_6O_3$	102.08	Acyclic	methoxy, carbonyl
4	3.27	Spiro[3.3]heptane-2,6-dione	$C_7H_8O_2$	124.13	Alicyclic	carbonyl
5	3.84	Furan-2-carbaldehyde	$C_5H_4O_2$	96.09	heterocyclic	aldehyde
6	3.99	4-hydroxy-4-methylpentan-2-one	$C_6H_{12}O_2$	116.16	Acyclic	carbonyl, hydroxyl
7	4.29	1,6:2,3-Dianhydro-4-*O*-acetyl-.beta.-D-allopyranose	$C_8H_{10}O_5$	186.16	heterocyclic	carbonyl, methoxy
8	4.35	methyl 3-hydroxyhexanoate	$C_7H_{14}O_3$	146.18	Acyclic	carbonyl, methoxy, hydroxyl
9	4.53	3-methylpent-4-en-2-one	$C_6H_{10}O$	98.15	Acyclic	carbonyl, alkenyl
10	5.42	2-methylcyclopent-2-en-1-one	C_6H_8O	96.13	Alicyclic	carbonyl, alkenyl
11	5.63	2*H*-furan-5-one	$C_4H_4O_2$	84.07	heterocyclic	carbonyl, alkenyl
12	5.92	2-hydroxycyclopent-2-en-1-one	$C_5H_6O_2$	98.10	Alicyclic	carbonyl, hydroxyl
13	7.07	5-methylfuran-2-carbaldehyde	$C_6H_6O_2$	110.11	Hetero-aromatic	aldehyde
14	7.57	3-methyl-2*H*-furan-2-one	$C_5H_6O_2$	98.10	heterocyclic	carbonyl
15	7.75	Phenol	C_6H_6O	94.11	Aromatic	phenyl
16	8.21	3,4-dihydroxycyclobut-3-ene-1,2-dione	$C_4H_2O_4$	114.06	Alicyclic	carbonyl, hydroxyl, alkenyl
17	9.15	1-methyl-2-propan-2-ylbenzene	$C_{10}H_{14}$	134.22	Aromatic	phenyl, alkyl
18	9.32	3-methylcyclopentane-1,2-dione	$C_6H_{10}O_3$	130.14	Alicyclic	carbonyl
19	10.42	2-methylphenol	C_7H_8O	108.14	Aromatic	phenyl, alkyl
20	11.30	4-methylphenol	C_7H_8O	108.14	Aromatic	phenyl, alkyl
21	11.70	2-methoxyphenol	$C_7H_8O_2$	124.14	Aromatic	phenyl, methoxy
22	11.93	4-Hydroxy Dihydro-2(3*H*)-furanone	$C_4H_6O_3$	102.08	heterocyclic	carbonyl, hydroxyl
23	15.76	3,3-dimethyloxetan-2-one	$C_5H_8O_2$	100.12	heterocyclic	carbonyl
24	16.09	4-methylphenol	$C_8H_{10}O_2$	138.17	Aromatic	phenyl, methoxy
25	18.15	5-(hydroxymethyl) furan-2-carbaldehyde	$C_6H_6O_3$	126.11	Heteroaromatic	aldehyde, hydroxyl
26	19.80	4-ethyl-2-methoxyphenol	$C_9H_{12}O_2$	152.19	Aromatic	phenyl, methoxy
27	21.28	4-ethenyl-2-methoxyphenol	$C_9H_{10}O_2$	150.18	Aromatic	phenyl, methoxy, alkenyl
28	23.14	2-methoxy-4-(prop-2-en-1-yl) phenol	$C_{10}H_{12}O_2$	164.20	Aromatic	phenyl, methoxy, alkenyl
29	23.55	2-methoxy-4-propylphenol	$C_{10}H_{14}O_2$	166.22	Aromatic	phenyl, methoxy, alkyl
30	24.85	4-Hydroxy-3-methoxybenzaldehyde	$C_8H_8O_3$	152.15	Aromatic	phenyl, methoxy, aldehyde
31	25.24	2-methoxy-4-[(*Z*)-prop-1-enyl]phenol	$C_{10}H_{12}O_2$	164.20	Aromatic	phenyl, methoxy, alkenyl
32	26.96	2-methoxy-4-[(*E*)-prop-1-enyl]phenol	$C_{10}H_{12}O_2$	164.20	Aromatic	phenyl, methoxy, alkenyl
33	28.41	1-(4-hydroxy-3-methoxyphenyl)ethan-1-one	$C_9H_{10}O_3$	166.18	Aromatic	phenyl, methoxy, aldehyde
34	30.21	1-(4-hydroxy-3-methoxyphenyl)propan-2-one	$C_{10}H_{12}O_3$	180.20	Aromatic	phenyl, methoxy, aldehyde
35	37.66	(*E*)-3-(4-hydroxy-3-methoxyphenyl)prop-2-enal	$C_{10}H_{10}O_3$	178.19	Aromatic	Phenyl, Methoxy, Aldehyde, Alkenyl
36	62.40	methyl 1,4a-dimethyl-9-oxo-7-propan-2-yl-3,4,10,10a-tetrahydro-2*H*-phenanthrene-1-carboxylate	$C_{21}H_{28}O_3$	328.20	Aromatic Polycyclic	Phenyl, Carbonyl,Methoxy, Alkyl
37	64.14	2-(3-hydroxy-4-methoxyphenyl)-5,6,7-trimethoxychromen-4-one	$C_{19}H_{18}O_7$	358.11	Aromatic, hereroaromatic Polycyclic	Phenyl, Carbonyl,Methoxy

Table 3
Main products from pine sawdust pyrolysis under concentrated solar light.

	425 suns		465 suns		550 suns		600 suns	
	Area (%)	IUPAC name	Area (%)	IUPAC name	Area (%)	IUPAC name	Area (%)	IUPAC name
1	1.55	toluene	5.07	toluene	2.05	Toluene	1.9	toluene
2	13.33	furan-2-carbaldehyde	20.38	furan-2-carbaldehyde	12.47	furan-2-carbaldehyde	17.16	furan-2-carbaldehyde
3	4.04	furan-2-ylmethanol	4.23	furan-2-ylmethanol	3.29	furan-2-ylmethanol	5.05	furan-2-ylmethanol
4	1.26	phenol	1.72	phenol	1.47	phenol	1.62	phenol
5	6.71	2-methoxyphenol	7.37	2-methoxyphenol	6.28	2-methoxyphenol	7.91	2-methoxyphenol
6	10.04	2-methoxy-4-methylphenol	7.37	2-methoxy-4-methylphenol	11.37	2-methoxy-4-methylphenol	11.02	2-methoxy-4-methylphenol
7	4.38	4-ethenyl-2-methoxyphenol	3.77	4-ethenyl-2-methoxyphenol	4.21	4-ethenyl-2-methoxyphenol	4.39	4-ethenyl-2-methoxyphenol
8	6.83	2-methoxy-4-[(e)-prop-1-enyl]phenol	5.92	2-methoxy-4-[(e)-prop-1-enyl]phenol	5.63	2-methoxy-4-[(E)-prop-1-enyl]phenol	6.65	2-methoxy-4-[(e)-prop-1-enyl] phenol

separated into different fuels. In this research, special attention was given to its value as a chemical production resource. The product was analyzed by GC mass spectroscopy and the results are provided in Fig. 8. The main types of liquid compounds in the product are xylene, styrene, phenols, naphthalene, and cresols. Chemical species evolve with solar fluxes. Table 2 lists the products obtained from solar powered pyrolysis for 301 suns. The products such as 2-oxopropanoic acid, methyl 2-oxopropanoate (known as 'methyl pyruvate'), furan-2-carbaldehyde (known as 'furfural'), 2-methoxyphenol (known as 'guaiacol'), and 4-hydroxy-3-methoxybenzaldehyde (known as 'vanillin') are widely used as flavoring agents [29]. Some of them are well-known antioxidants such as 4-methylphenol [30], 2-methoxy-4-(prop-2-en-1-yl) phenol [31], and 2-(3-hydroxy-4-methoxyphenyl)-5,6,7-trimethoxychromen-4-one [32]. Also antiseptic 2-methoxy-4-(prop-2-en-1-yl) phenol [33] is present in the product. Importantly, compounds used for manufacturing medicines, including asmathitic 1-(4-hydroxy-3-methoxyphenyl) ethan-1-one [34] and anticancer 3,4-dihydroxycyclobut-3-ene-1,2-dione, are also found in the product [35]. Only major products resulting from other solar intensities are reported, as shown in Table 3.

Table 3 lists the main bio-oil components from pine sawdust pyrolysis at different solar light intensities. The main higher yield

Table 4
Main products from pine sawdust pyrolysis using electrical heating.

	450 °C		500 °C		550 °C	
	Area (%)	IUPAC name	Area (%)	IUPAC name	Area (%)	IUPAC name
1	3.69	methyl acetate	3.38	methyl acetate	3.56	methyl acetate
2	4.72	furan-2-carbaldehyde	3.98	furan-2-carbaldehyde	4.01	furan-2-carbaldehyd
3	3.46	furan-2-ylmethanol	2.54	furan-2-ylmethanol	2.27	furan-2-ylmethanol
4	3.70	cyclopentane-1,2-dione	3.60	cyclopentane-1,2-dione	3.65	cyclopentane-1,2-dione
5	5.06	2-methoxyphenol	4.81	2-methoxyphenol	4.97	2-methoxyphenol
6	4.29	N'-methylpropane-1,3-diamine	3.25	N'-methylpropane-1,3-diamine	2.77	N'-methylpropane-1,3-diamine
7	6.72	4-ethenyl-2-methoxyphenol	6.89	4-ethenyl-2-methoxyphenol	6.95	4-ethenyl-2-methoxyphenol
8	5.45	4-ethenyl-2-methoxyphenol	5.53	4-ethenyl-2-methoxyphenol	5.60	4-ethenyl-2-methoxyphenol
9	5.53	2-methoxy-4-[(E)-prop-1-enyl]phenol	5.84	2-methoxy-4-[(E)-prop-1-enyl]phenol	5.54	2-methoxy-4-[(E)-prop-1-enyl]phenol

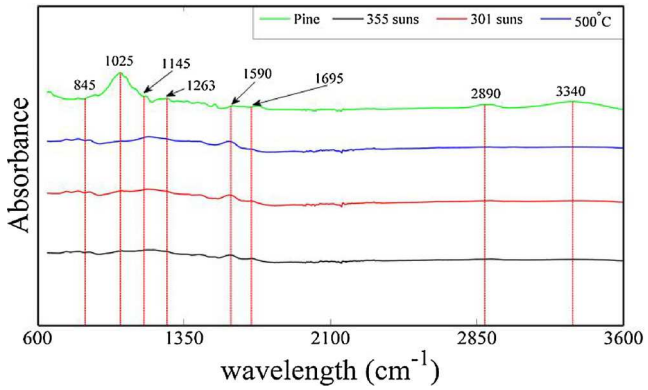

Fig. 9. FTIR of pine and pine-char. [a: — pure pine sawdust at ambient condition; b: — pine-char produced in an electrically heated reactor at 500 °C; c: — pine-char produced in a solar reactor at 301 suns flux; d: — pine-char produced in a solar reactor at 355 suns flux].

compounds (area percentage more than 4%) are toluene, furan-2-carbaldehyde, furan-2-ylmethanol, 2-methoxyphenol, 2-methoxy-4-methylphenol, 4-ethenyl-2-methoxyphenol,2-methoxy-4-[(e)-prop-1-enyl] phenol.

Table 4 lists the main bio-oil components from pine sawdust pyrolysis at different temperatures. Zhao et al. from the same research group described the experimental setup and methodology of this analysis [36]. However, no water was added with carrier nitrogen gas and the pyrolysis was performed without using any catalyst. The main higher yield compounds (area percentage more than 3%) are methyl acetate, furan-2-carbaldehyde, furan-2-ylmethanol, cyclopentane-1, 2-dione, 2-methoxyphenol, N'-methylpropane-1,3-diamine, 4-ethenyl-2-methoxyphenol, 4-ethenyl-2-methoxyphenol, 2-methoxy-4-[(E)-prop-1-enyl]phenol. It is evident that concentrated solar light facilitates production of furan derivatives and phenolic compounds.

3.6. FTIR analysis of bio char

In Fig. 9, the FTIR spectra is presented for four different samples – pine sawdust, pine char produced under 355 suns flux, pine char produced under 301 suns flux, and pine char produced in electrically heated reactor. The bond characteristics of pine char using different type of heating method in FTIR spectra region of 500–3500 cm^{-1} looks identical. The −OH band around 3340 cm^{-1} for pine sawdust does not show up in pine char. A similar statement can be made for C−H stretching vibration (2890 cm^{-1}), aromatic C=C stretching modes (1263 cm^{-1}), and C−O stretching (1025 cm^{-1}). However, a strong peak appears at 1590 $cm^{-1}$for pine char. A small peak corresponds to $-CH_2$ out-of-plane bending vibration also appears for biochar at 845 cm^{-1}. Zhao et al. described the formation and termination of different functional groups for pinewood at different temperature (100 °C to 600 °C) [37].

4. Conclusion

A simple but novel biomass pyrolysis scheme is developed by using a 5KW solar simulator can produce irradiance with stable spectral characteristics. The solar flux profiles at different distances from the solar simulator vary with input powers. It has been shown that the solar flux map is uniform on a plane 28.5 cm away from the simulator. The stable solar flux can be achieved within a short illumination start time (2–4 min) with very little (± 5%) fluctuations. Furthermore, the flux profiles can be successfully modeled by using Soltrace® software based on the first law of thermodynamics to validate the performance of the solar simulator. Moreover, the solar simulator can produce enough irradiance to heat the reactants up to 900 °C for pyrolyzing carbonaceous materials. The bio-oil produced with the pyrolysis of pinewood can be separated into useful fuels and chemicals. It is observed that, concentrated solar light can improve the production of phenolic compounds. The characteristics of the products using the solar simulator powered biomass pyrolysis imply that solar energy can effectively replace the electrical heating for producing value-added materials from bioresources.

Acknowledgement

The authors thank the State of Wyoming and the National Science Foundation (NSF OIA-1632899) for their support to this research.

Appendix A

Solar flux measurement procedure

The radiation intensity, angle of incidence, and position of the focal point can be adjusted using controls located on the solar simulator and rectifier. To prevent bodily injury or damage to the equipment, a list of recommended personal protective equipment and lab safety equipment was created and detailed operation procedure for the simulator was established. Before starting the operation, it should be made sure that the connection between the exhaust fans to fume hood is on, all switches are turned off, and the dousing plate is closed. The booster fan, rectifier, lamp housing, and cooling fan should be powered to turn on in sequence. The lamp should be switched on after donning safety glasses. The power and focus position is adjusted before opening the dousing plate. After that, the dousing plate is lowered to expose solar light at the target and the needed operation is performed (e.g., the pyrolysis experiment, flux measurements, etc.). After the experiment is completed, the lamp house should be powered off. After

providing 15 min for the system to cool down, the other connections or switches are turned off following the reverse sequence previously followed.

Several steps are necessary to focus the concentrated solar light at a certain position. First, the adjustable rod is placed and secured in front of the reactor. Second, the length of the rod is adjusted to the desired size and the solar flux measurement system is placed in such a way that the sensor touches the tip of the rod. To run the pyrolysis experiment, the reactor is put in place of the sensor described here. Finally, the rod is removed without changing the position of the sensor or reactor.

To measure the flux, the solar lamp is first turned on and aimed at the sensor. The sensor position is changed using the vertical and horizontal screws. The horizontal position is initially fixed and the change of flux in the vertical direction is measured while the sensor with the backing plate is moved gradually. The sensor is then moved towards the horizontal position slightly prior to repeating the entire process. Measurements are taken both in X- and Y-directions at 1 mm intervals. Flux is measured at more than 1000 nodes. The input power, focus position, and Z-distance are kept constant during the operation. After measuring the flux distribution at a certain power level, the input power is changed using the two power controller screws to measure the spatial variance of solar flux at that power level. The position of the flux measurement sensor is changed using the adjustable rod to measure the flux variance at different power levels at different distances from the solar simulator.

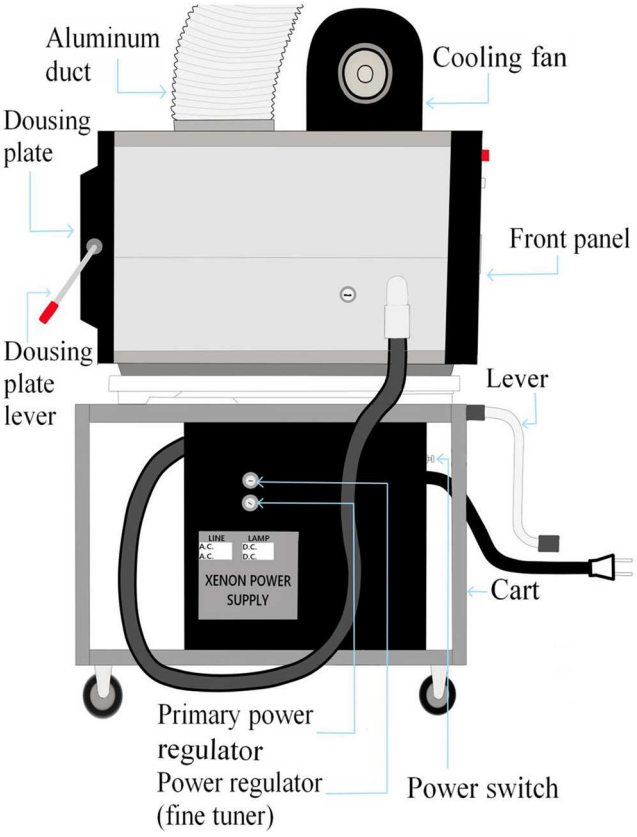

Fig. A1. Solar Simulator Secured to Scissor Lift and Soft Ride Utility Cart (Side View).

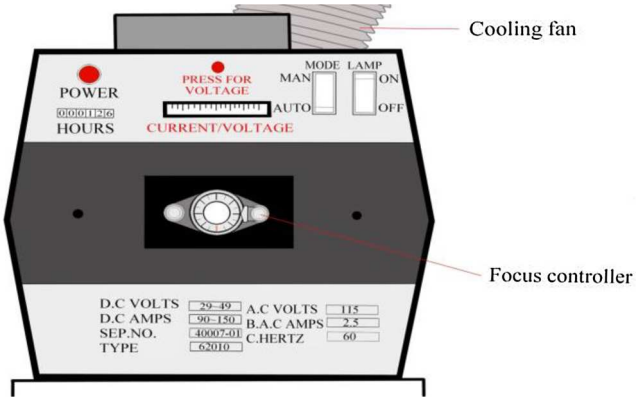

Fig. A2. Front Panel of solar simulator.

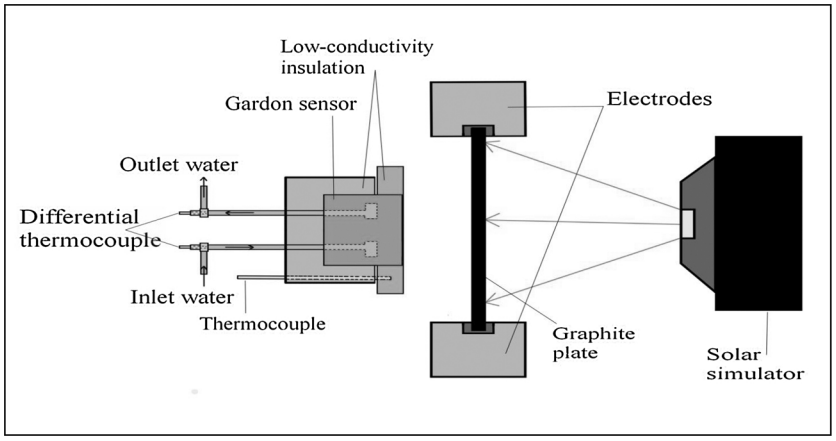

Fig. A3. Schematic of Gardon Gauge.

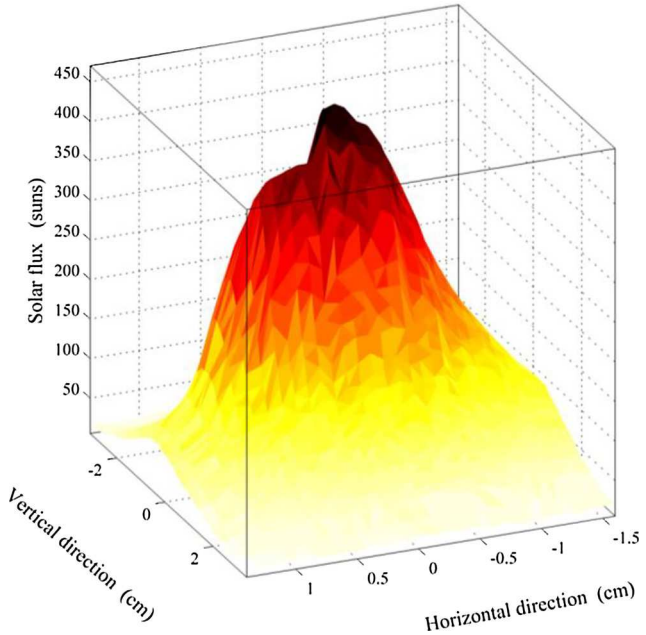

Fig. A4. Solar flux at 130A (avg.) measured on a plane 26.5 cm away from the solar simulator.

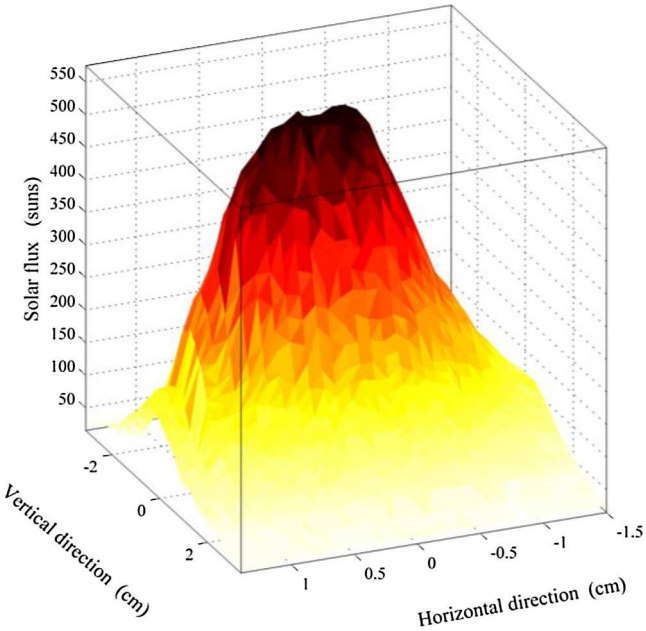

Fig. A5. Solar flux at 150A (avg.) measured on a plane 26.5 cm away from the solar simulator.

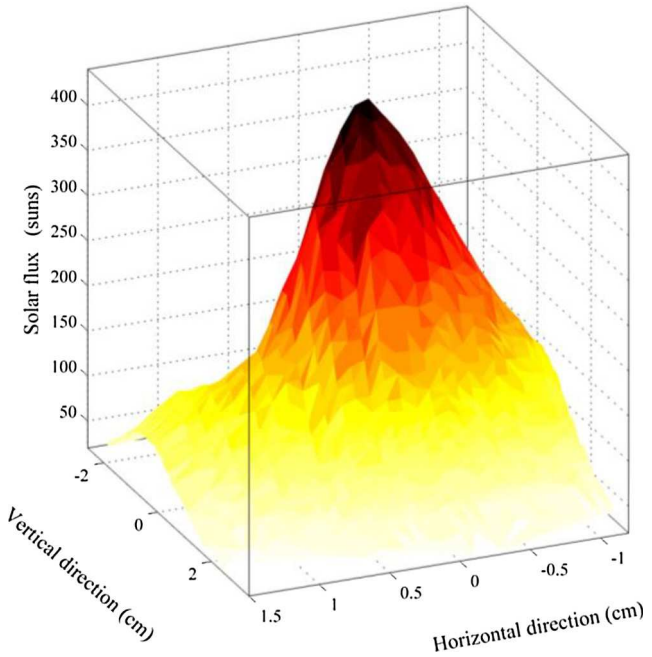

Fig. A6. Solar flux at 130A (avg.) measured on a plane 28.5 cm away from the solar simulator.

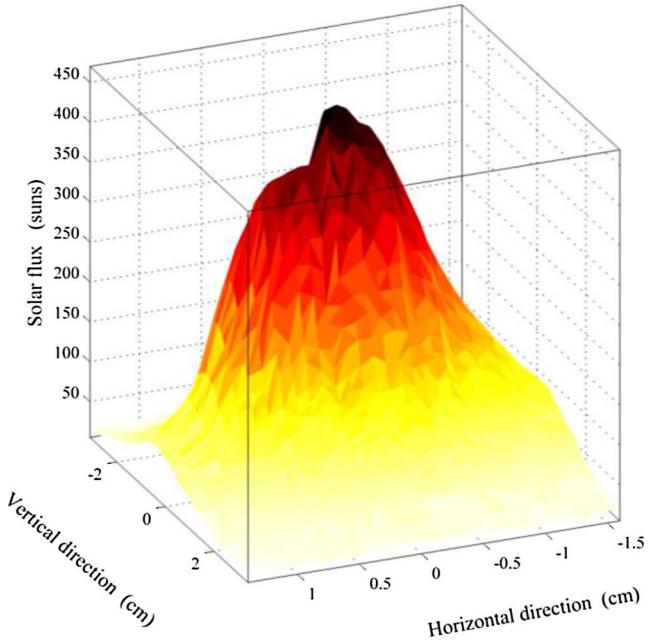

Fig. A7. Solar flux at 130A (avg.) measured on a plane 30.5 cm away from the solar simulator.

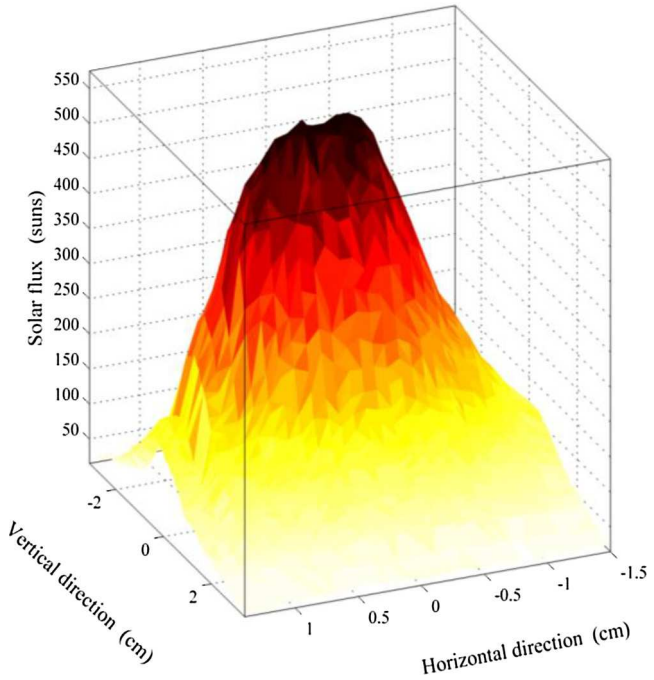

Fig. A8. Solar flux at 155A (avg.) measured on a plane 30.5 cm away from the solar simulator.

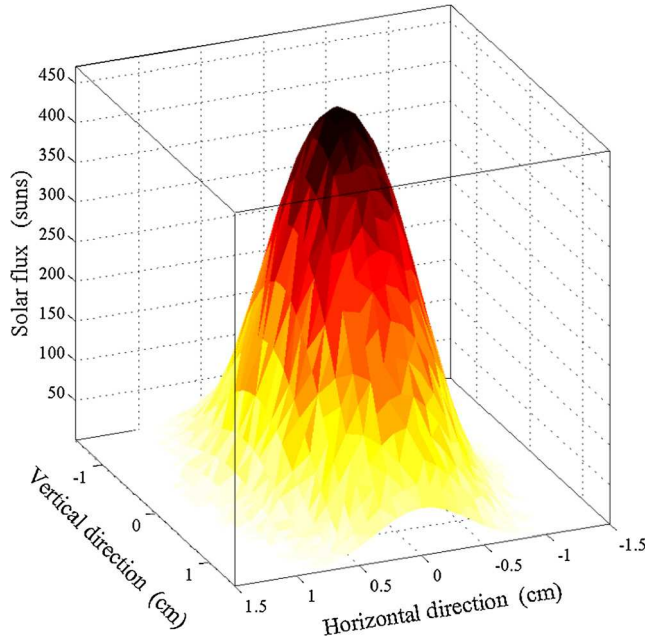

Fig. A9. Solar flux map on a plane 26.5 cm away from the solar simulator modeled using Solrtace®. Flux map is comparable to Fig. A4.

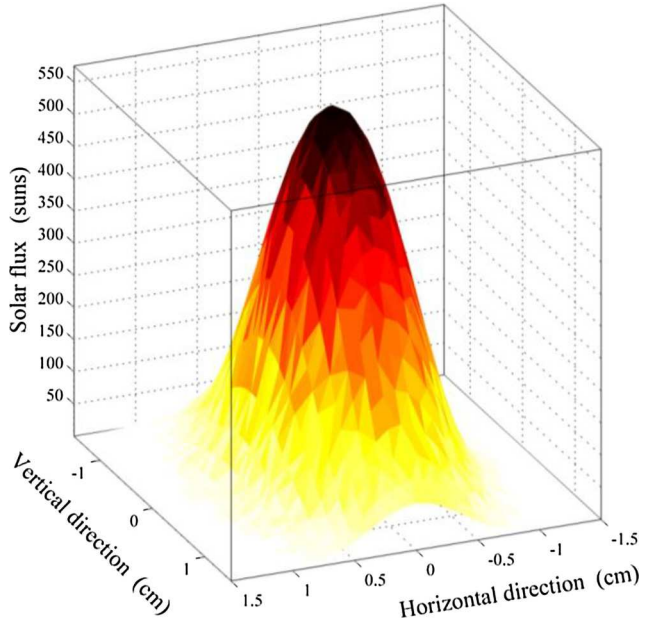

Fig. A10. Solar flux map on a plane 26.5 cm away from the solar simulator modeled using Solrtace®. Flux map is comparable to Fig A5.

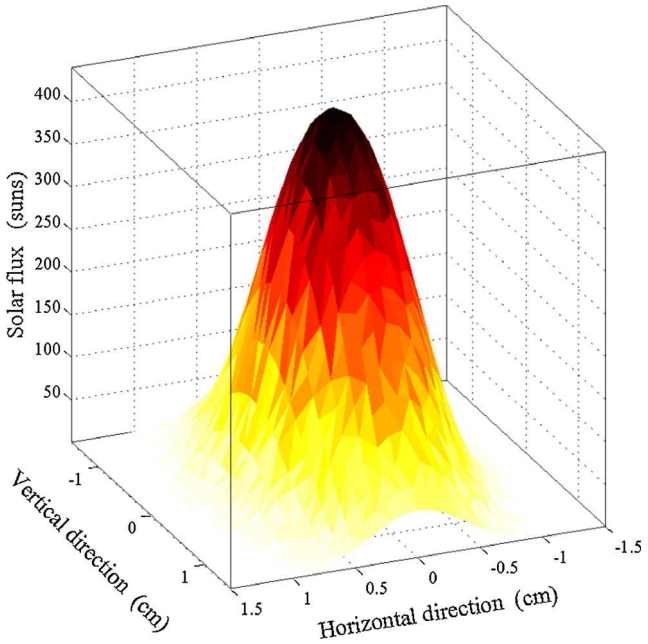

Fig. A11. Solar flux map on a plane 28.5 cm away from the solar simulator modeled using Solrtace®. Flux map is comparable to Fig. A6.

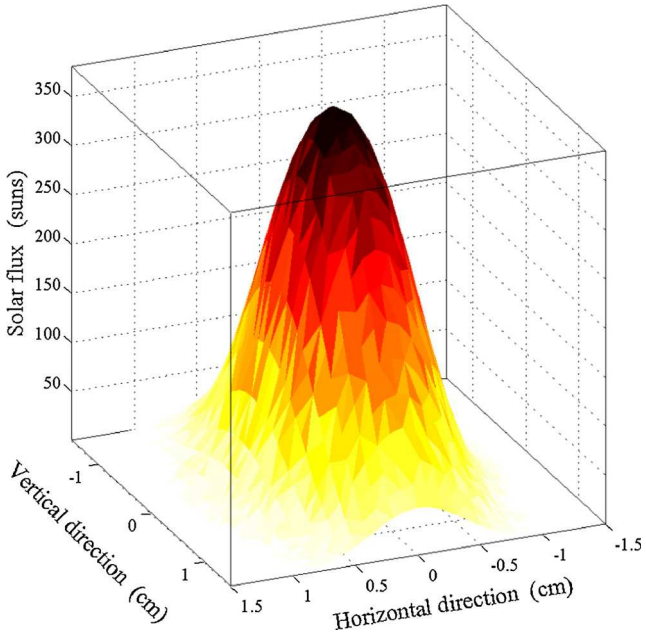

Fig. A12. Solar flux map on a plane 30.5 cm away from the solar simulator modeled using Solrtace®. Flux map is comparable to Fig. A7.

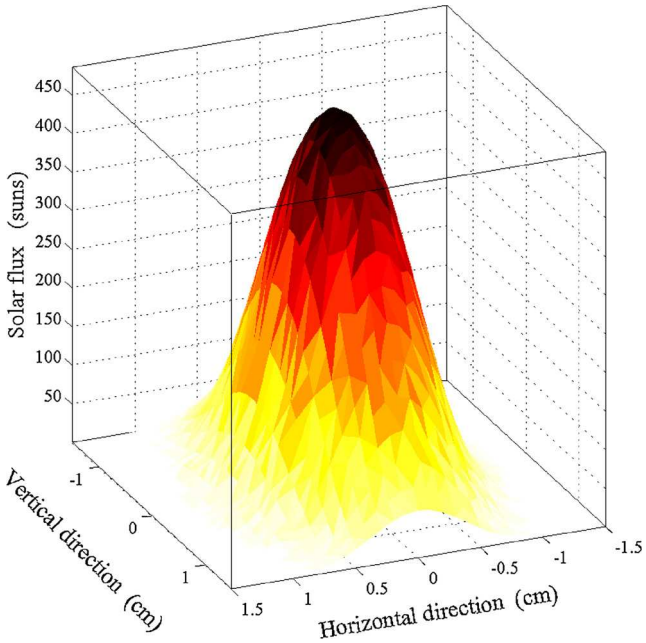

Fig. A13. Solar flux map on a plane 30.5 cm away from the solar simulator modeled using Solrtace®. Flux map is comparable to Fig. A8.

References

[1] B. Hartweg, Global implementation of renewable energy, in: M.R.C. Keith, E. Peterman, Gregory P. Foy (Eds.), Clim. Chang. Lit. Educ. Soc. Justice, Energy, Econ. Paris Agreem. 2017, pp. 81–90, , http://dx.doi.org/10.1021/bk-2017-1254.ch007.

[2] M. Asif, T. Muneer, Energy supply, its demand and security issues for developed and emerging economies, Renew. Sustain. Energy Rev. 11 (2007) 1388–1413, http://dx.doi.org/10.1016/j.rser.2005.12.004.

[3] N.S. Lewis, D.G. Nocera, Powering the planet: chemical challenges in solar energy utilization, Proc. Natl. Acad. Sci. U. S. A. 103 (2006) 15729–15735, http://dx.doi.org/10.1073/pnas.0603395103.

[4] K. Zeng, D. Gauthier, J. Soria, G. Mazza, G. Flamant, Solar pyrolysis of carbonaceous feedstocks: a review, Sol. Energy 156 (2017) 73–92, http://dx.doi.org/10.1016/J.SOLENER.2017.05.033.

[5] J. Milano, H.C. Ong, H.H. Masjuki, W.T. Chong, M.K. Lam, P.K. Loh, V. Vellayan, Microalgae biofuels as an alternative to fossil fuel for power generation, Renew. Sustain. Energy Rev. 58 (2016) 180–197, http://dx.doi.org/10.1016/J.RSER.2015.12.150.

[6] A. Abubakar Mas'ud, A.V. Wirba, F. Muhammad-Sukki, R. Albarracín, S.H. Abu-Bakar, A.B. Munir, N.A. Bani, A review on the recent progress made on solar photovoltaic in selected countries of sub-Saharan Africa, Renew. Sustain. Energy Rev. 62 (2016) 441–452, http://dx.doi.org/10.1016/J.RSER.2016.04.055.

[7] C.L. Azimoh, P. Klintenberg, F. Wallin, B. Karlsson, Illuminated but not electrified: an assessment of the impact of solar home system on rural households in South Africa, Appl. Energy 155 (2015) 354–364, http://dx.doi.org/10.1016/J.APENERGY.2015.05.120.

[8] F.C. Ertem, P. Neubauer, S. Junne, Environmental life cycle assessment of biogas production from marine macroalgal feedstock for the substitution of energy crops, J. Clean. Prod. 140 (2017) 977–985, http://dx.doi.org/10.1016/J.JCLEPRO.2016.08.041.

[9] N. Piatkowski, C. Wieckert, A.W. Weimer, A. Steinfeld, Solar-driven gasification of carbonaceous feedstock—a review, Energy Environ. Sci. 4 (2011) 73–82, http://dx.

doi.org/10.1039/C0EE00312C.
[10] T. Kodama, High-temperature solar chemistry for converting solar heat to chemical fuels, Prog. Energy Combust. Sci. 29 (2003) 567–597, http://dx.doi.org/10.1016/S0360-1285(03)00059-.
[11] D. Bickler, The simulation of solar radiation, Sol. Energy 6 (1962) 64–68, http://dx.doi.org/10.1016/0038-092X(62)90006-3.
[12] ASTM E927-10(2015) Standard Specification for Solar Simulation for Photovoltaic Testing, (2015), http://dx.doi.org/10.1520/E0927-10R15 West Conshohocken, PA.
[13] X. Dong, Z. Sun, G.J. Nathan, P.J. Ashman, D. Gu, Time-resolved spectra of solar simulators employing metal halide and xenon arc lamps, Sol. Energy 115 (2015) 613–620, http://dx.doi.org/10.1016/j.solener.2015.03.017.
[14] W. Wang, Simulate a Sun for Solar Research: A Literature Review of Solar Simulator Technology, Stockholm, Sweden, 2014. https://www.diva-portal.org/smash/get/diva2:756274/FULLTEXT01.pdf (Accessed 20 September 2016).
[15] S. Morales, R. Miranda, D. Bustos, T. Cazares, H. Tran, Solar biomass pyrolysis for the production of bio-fuels and chemical commodities, J. Anal. Appl. Pyrolysis 109 (2014) 65–78, http://dx.doi.org/10.1016/j.jaap.2014.07.012.
[16] A.V. Bridgwater, Review of fast pyrolysis of biomass and product upgrading, Biomass Bioenergy 38 (2012) 68–94, http://dx.doi.org/10.1016/j.biombioe.2011.01.048.
[17] M. Gavrilescu, Biomass potential for sustainable environment, biorefinery products and energy, in: I. Visa (Ed.), Sustain. Energy Built Environ.—Steps Towar. nZEB Proc. Conf. Sustain. Energy 2014, Springer International Publishing, Cham, 2014, pp. 169–194, , http://dx.doi.org/10.1007/978-3-319-09707-7_13.
[18] R. Li, K. Zeng, J. Soria, G. Mazza, D. Gauthier, R. Rodriguez, G. Flamant, Product distribution from solar pyrolysis of agricultural and forestry biomass residues, Renew. Energy 89 (2016) 27–35, http://dx.doi.org/10.1016/j.renene.2015.11.071.
[19] R. Zanzi, K. Sjöström, E. Björnbom, Rapid high-temperature pyrolysis of biomass in a free-fall reactor, Fuel 75 (1996) 545–550, http://dx.doi.org/10.1016/0016-2361(95)00304-5.
[20] B. Shrestha, Y. le Brech, T. Ghislain, S. Leclerc, V. Carré, F. Aubriet, S. Hoppe, P. Marchal, S. Pontvianne, N. Brosse, A. Dufour, A multitechnique characterization of lignin softening and pyrolysis, ACS Sustain. Chem. Eng. 5 (2017) 6940–6949, http://dx.doi.org/10.1021/acssuschemeng.7b01130.
[21] T. Kan, V. Strezov, T.J. Evans, Lignocellulosic biomass pyrolysis: a review of product properties and effects of pyrolysis parameters, Renew. Sustain. Energy Rev. 57 (2016) 1126–1140, http://dx.doi.org/10.1016/J.RSER.2015.12.185.
[22] L. Guo, H. Jin, Y. Lu, Supercritical water gasification research and development in China, J. Supercrit. Fluids 96 (2015) 144–150, http://dx.doi.org/10.1016/J.SUPFLU.2014.09.023.
[23] J. Chen, Y. Lu, X. Zhang, P. Xiao, Hydrogen production by biomass gasification in supercritical water using concentrated solar energy: system development and proof of concept, Int. J. Hydrogen Energy 35 (2010) 7134–7141, http://dx.doi.org/10.1016/J.IJHYDENE.2010.02.023.
[24] ASTM D3172-13 Standard Practice for Proximate Analysis of Coal and Coke, (2013), http://dx.doi.org/10.1520/D3172 West Conshohocken, PA.
[25] J. Ballestrín, C.A. Estrada, M. Rodríguez-Alonso, C. Pérez-Rábago, L.W. Langley, A. Barnes, Heat flux sensors: calorimeters or radiometers? Sol. Energy 80 (2006) 1314–1320, http://dx.doi.org/10.1016/j.solener.2006.03.005.
[26] J. Ballestrín, S. Ulmer, A. Morales, A. Barnes, L. Langley, M. Rodríguez, Systematic error in the measurement of very high solar irradiance, Sol. Energy Mater. Sol. Cells 80 (2003) 375–381, http://dx.doi.org/10.1016/J.SOLMAT.2003.08.014.
[27] T. Wendelin, SolTRACE: a new optical modeling tool for concentrating solar optics, Sol. Energy, ASME, Kohala Coast, Hawaii, USA, 2003, pp. 253–260, http://dx.doi.org/10.1115/ISEC2003-44090.
[28] T. Wendelin, A. Dobos, A. Lewandowski, SolTrace. A Ray-Tracing Code for Complex Solar Optical Systems, 2013. https://www.nrel.gov/docs/fy14osti/59163.pdf (Accessed 6 December 2017).
[29] Henry B. Heath, Source Book of Flavors: (AVI Sourcebook and Handbook Series) – Henry B. Heath – Google Books, 1st ed., Springer, 1981.
[30] J. Vichapong, M. Sookserm, V. Srijesdaruk, P. Swatsitang, S. Srijaranai, High performance liquid chromatographic analysis of phenolic compounds and their antioxidant activities in rice varieties, LWT—Food Sci. Technol. 43 (2010) 1325–1330, http://dx.doi.org/10.1016/J.LWT.2010.05.007.
[31] M. OGATA, M. HOSHI, S. URANO, T. ENDO, Antioxidant activity of eugenol and related monomeric and dimeric compounds, Chem. Pharm. Bull. (Tokyo) 48 (2000) 1467–1469, http://dx.doi.org/10.1248/cpb.48.1467.
[32] G. Akowuah, I. Zhari, I. Norhayati, A. Sadikun, S. Khamsah, Sinensetin, eupatorin, 3′-hydroxy-5, 6, 7, 4′-tetramethoxyflavone and rosmarinic acid contents and antioxidative effect of Orthosiphon stamineus from Malaysia, Food Chem. 87 (2004) 559–566, http://dx.doi.org/10.1016/J.FOODCHEM.2004.01.008.
[33] S. Abbaszadeh, A. Sharifzadeh, H. Shokri, A.R. Khosravi, A. Abbaszadeh, Antifungal efficacy of thymol, carvacrol, eugenol and menthol as alternative agents to control the growth of food-relevant fungi, J. Mycol. Med. 24 (2014) e51–e56, http://dx.doi.org/10.1016/J.MYCMED.2014.01.063.
[34] B.A. 'T Hart, J.M. Simons, K.-S. Shoshan, N.P.M. Bakker, R.P. Labadie, Antiarthritic activity of the newly developed neutrophil oxidative burst antagonist apocynin, Free Radic. Biol. Med. 9 (1990) 127–131, http://dx.doi.org/10.1016/0891-5849(90)90115-Y.
[35] L.F. Tietze, M. Arlt, M. Beller, K.-H. Gl üsenkamp, E. Jähde, M.F. Rajewsky, Anticancer agents, 15. Squaric Acid Diethyl Ester: A New Coupling Reagent for the Formation of Drug Biopolymer Conjugates. Synthesis of squaric acid ester amides and diamides, Chem. Ber. 124 (1991) 1215–1221, http://dx.doi.org/10.1002/cber.19911240539.
[36] J. Chen, Y. Lu, X. Zhang, P. Xiao, Hydrogen production by biomass gasification in supercritical water using concentrated solar energy: system development and proof of concept, Int. J. Hydrogen Energy 35 (2010) 7134–7141, http://dx.doi.org/10.1016/J.IJHYDENE.2010.02.023.
[37] Z. Sun, B. Xu, A.H. Rony, S. Toan, S. Chen, K.A.M. Gasem, H. Adidharma, M. Fan, W. Xiang, Thermogravimetric and kinetics investigation of pine wood pyrolysis catalyzed with alkali-treated CaO/ZSM-5, Energy Convers. Manage. 146 (2017) 182–194, http://dx.doi.org/10.1016/J.ENCONMAN.2017.04.104.